Systematic Airfoil Design Studies at Low Reynolds Numbers

Michael S. Selig,* Ashok Gopalarathnam,† Philippe Giguère,‡ and Christopher A. Lyon§
University of Illinois at Urbana-Champaign, Urbana, Illinois

Nomenclature

C_l = lift coefficient, chord = 1
H_{12} = boundary-layer shape factor δ_1/δ_2
α = airfoil angle of attack relative to chord line
α^* = segment design angle of attack relative to zero-lift line
α_z = airfoil angle of attack relative to zero-lift line
α_{zl} = airfoil zero-lift angle of attack
δ_1 = boundary-layer displacement thickness
δ_2 = boundary-layer momentum thickness
ϕ = segment arc limit used in conformal mapping

Subscripts

x_r = chordwise laminar bubble reattachment location
x_s = chordwise laminar-separation location
x_{tr} = chordwise transition location

I. Introduction

FOR over 100 years, airfoil design has continued to capture the interest of practitioners of applied aerodynamics. The field is fueled by the ever-growing

*Associate Professor, Department of Aeronautical and Astronautical Engineering. Senior Member AIAA.

†Graduate Research Assistant, Department of Aeronautical and Astronautical Engineering; currently Assistant Professor, Department of Mechanical and Aerospace Engineering, North Carolina State University. Member AIAA.

‡Graduate Research Assistant, Department of Aeronautical and Astronautical Engineering; currently Senior Aerodynamicist, Enron Wind Corp. Member AIAA.

§Graduate Research Assistant, Department of Aeronautical and Astronautical Engineering; currently Software and Aerospace Engineer, Frasca International. Member AIAA.

combination of airfoil design requirements for unique applications, and this state of affairs is not likely to change. When one considers all possible permutations of the myriad airfoil design requirements, it quickly becomes apparent that the number of unique sets of requirements far exceeds the collection of existing airfoils. For this reason, the advancement and use of methods for airfoil design continues to be the economical solution. In contrast, the enrichment of airfoil "catalogs" for their own sake is felt to be of limited value.

The objective of this chapter derives from two topics. First, the alternative to our great legacy of airfoil design by geometric means guided by empirical study is to use an inverse method, and there are certain advantages to be had by adopting the latter while realizing that often geometric constraints must still be achieved. By adopting an inverse approach, the degree to which the aerodynamic performance can be controlled has reached a high level of sophistication, and this can be illustrated clearly by examples. Second, inverse design in the classic sense involves specifying a desired velocity distribution based on boundary-layer considerations. Taking this one step further by directly prescribing the desired boundary-layer characteristics is a step closer to controlling the desired outcome—the performance. Thus, employing an inverse boundary-layer-like approach can give the designer tremendous power in achieving the performance goals in the face of all the tradeoffs that one must consider in the process of airfoil design. These two aspects of a modern inverse airfoil design methodology form the subject of this chapter: design via boundary-layer considerations in an inverse sense.

To illustrate this approach, three series of low Reynolds number airfoils are presented. In each case, state-of-the-art tools for airfoil design[1,2] and analysis[3–5] were used. Although these airfoils were each designed for specific applications, the systematic and parametric studies show useful performance trends and tradeoffs in airfoil design at low Reynolds numbers. As will be shown, the overall design process has been validated through wind tunnel tests, and these results are presented together with the predictions.

II. Design Process

As an overview, the design process proceeded as follows. PROFOIL[1,2] was first used for rapid and interactive design. A new airfoil that appeared to meet the performance objectives was then screened through experience and analysis using the Eppler code[3,4] and/or XFOIL[5] to obtain the lift, drag, and pitching moment characteristics of the airfoil over a range of angles of attack. If at any state the candidate airfoil failed to meet the design goals, that additional experience was used to redesign the airfoil to more closely match the desired performance. This iterative process continued until a successful airfoil was designed, at which point the design was built and wind-tunnel tested to evaluate its performance. A more detailed description of each of these elements of the process follows.

A. PROFOIL

The PROFOIL code[1,2] embodies an inverse airfoil design method and an integral boundary-layer method for rapid analysis at the design points. The method draws on the pioneering work of Eppler[3,4,6,7] in inverse airfoil design and analysis through conformal mapping and integral boundary-layer techniques, respectively.

PROFOIL differs from the Eppler code in that laminar and turbulent boundary-layer developments can be directly prescribed through iteration on the velocity distribution. The method also allows for control over certain geometric constraints, such as the local geometry, maximum thickness, and thickness distribution. Additional differences are discussed in Refs. 1, 2, and 8. Both the boundary layer and thickness-constraint capabilities are used in the examples here. More details of the method will be given with the design examples to follow. A Web-based version of PROFOIL and further discussion is available online at http://www.uiuc.edu/ph/www/m-selig (cited September 2001).

B. Eppler Code

As mentioned, the Eppler code[3] was used for first-stage screening of candidate airfoils. Thus, only the analysis mode is discussed. In the analysis mode, the inviscid velocity distributions are determined by an accurate third-order panel method. Performance is then determined through the use of an integral boundary-layer method using the inviscid velocity distribution, which makes the analysis exceptionally fast (0.03-s elapse time on a 600-MHz PC per polar). In the version of the code used for this work, the drag caused by a laminar separation bubble is not calculated. Although the magnitude of the bubble drag is not determined, the method is invaluable when the user has had experience comparing its predictions with experiments. For example, the code has been used to design several successful low Reynolds number airfoils that can be found in the literature.[9–15]

C. XFOIL

XFOIL[5] is a design and analysis method for subcritical airfoils. In the data presented here, XFOIL has been used as a postdesign viscous/inviscid analysis tool. A linear-vorticity second-order-accurate panel method is used for inviscid analysis in XFOIL. This panel method is coupled with an integral boundary-layer method and an approximate e^n-type transition amplification formulation using a global Newton method to compute the inviscid/viscous coupling, requiring approximately 15 s of elapse time per polar on a 600-MHz PC. XFOIL has proven to be well suited for the analysis of subcritical airfoils even in the presence of significant laminar-separation bubbles.

The XFOIL analyses in this work were used primarily to study tradeoffs and effects of systematic variations in airfoils and for selecting the most suitable candidates before wind tunnel testing. For this purpose, the value $n_{\text{crit}} = 9$ was found to be quite suitable based on prior experience with comparisons between XFOIL results and the University of Illinois open-return subsonic wind tunnel data. This value $n_{\text{crit}} = 9$ was used for transition prediction in the data presented here.

D. Wind-Tunnel Tests

This section describes the wind-tunnel experiments. Because details of the method can be found in Refs. 16, 17, and 18, only a summary is given here. The experiments were performed in the University of Illinois open-return subsonic wind tunnel. The rectangular test-section dimensions are approximately 2.8×4 ft in cross section and 8-ft-long. To ensure good flow quality in the test section, the

tunnel settling chamber contains a 4-in.-thick honeycomb and four antiturbulence screens, resulting in a turbulence level of less than 0.1% over the Reynolds number range tested.[16] The SA703x series models were made from hot-wire cut foam cores covered with fiberglass and resin under a mylar vacuum bag. The SG604x and S607x series models were from polyurethane RenShape®, milled using a numerically-controlled machine, then sanded and painted.

To isolate the ends of the airfoil model from the tunnel side-wall boundary layers and the outer support hardware, the airfoil models were mounted horizontally between two 3/8-in.-thick, 6-ft-long Plexiglas® splitter plates. Gaps between the model and splitter plates were nominally 0.05 in. All models had a 12 in. chord and 33 5/8-in. span. One side of the model was free to pivot. At this location, the angle of attack was measured using a potentiometer. The other side of the model was free to move vertically on a precision ground shaft, but it was not free to rotate. A loadcell restrained the motion of the model and measured the lift force. Linear and spherical ball bearings within the lift carriage helped to minimize any frictional effects.

The drag was obtained from the momentum method. To ensure that the wake had relaxed to tunnel static pressure, the wake measurements were performed 14.8 in. (approximately 1.25 chord lengths) downstream of the model trailing edge. Each vertical wake traverse consisted of between 20 and 80 total-head pressure measurements (depending on the wake thickness) with points nominally spaced 0.08 in. apart. Owing to spanwise wake nonuniformities,[19,20] wake profile measurements were taken at four spanwise locations spaced 4 in. apart over the center 12 in. of the model span. The resulting four drag coefficients were then averaged to obtain the drag at a given angle of attack.

The airfoil pitching moment was measured via a loadcell connected between two lever arms, one metric with the model and the other fixed to the lift carriage angle-of-attack adjustment plate.

The lift, drag, moment, and angle-of-attack measurements were corrected to account for the effects of solid blockage, wake blockage, and streamline curvature.[21] The velocity was not only corrected for solid and wake blockage but also for a "circulation effect" that is unique to setups that make use of splitter plates. For the current tests, the freestream velocity rather than being measured far upstream was measured between the splitter plates for higher accuracy. Because the pitot-static probe that was used to measure the freestream velocity was located fairly close to the model, the probe measurements were therefore corrected for airfoil circulation effects so as to obtain the true freestream test section speed. The details of this correction procedure can be found in Ref. 22.

Overall uncertainty in the lift coefficient is estimated to be 1.5%. The drag measurement error comes from three sources: accuracy of the data acquisition instruments, repeatability of the measurements, and the locations of the particular four wake profiles used to determine the average drag coefficient. Based partly on the error analysis method presented in Refs. 23 and 24, the uncertainty due to the instruments and measurement repeatability are less than 1% and 1.5%, respectively. Based on a statistical analysis (for a 95% confidence interval) of the spanwise drag results for the E374 airfoil[19] at $\alpha = 4$ deg, the uncertainties due to the spanwise variations were estimated to be approximately 1.5% at and above $Re = 200{,}000$. The current airfoils are expected to have approximately the same uncertainties. A more detailed discussion of this topic is presented in Ref. 20. For the angle-of-attack sensor, the uncertainty is estimated to be 0.08 deg.

To determine the accuracy of airfoil profiles, each model was digitized with a Brown and Sharpe coordinate measuring machine. Approximately 80 points were taken around each airfoil, and the spacing between points was approximately proportional to the local curvature. Thus, near the leading and trailing edges, the spacing was relatively small, whereas over the midchord it was no greater than 0.7 in. These measured coordinates were compared with the true coordinates using a two-dimensional least-squares approach (rotation and vertical translation), which yielded an average difference of approximately 0.010 in. or less for all airfoils discussed in this chapter.

Data taken on the E387 model for $Re = 200{,}000$ and 460,000 are presented in Ref. 16 and compares well with data taken in the NASA Langley low-turbulence pressure tunnel (LTPT).[23] Moreover, surface oil-flow visualization taken to determine the laminar separation and oil-accumulation lines showed that the lines agreed with NASA Langley LTPT data to within 1–2% of chord.[25] This good agreement serves to validate the current experiments.

III. Parametric Studies in Airfoil Design

In this section, three airfoil series are discussed with special emphasis given to the design process involving the aforementioned tools.

A. SA 703x Series

This first series is for application to radio-controlled (R/C) model aircraft, specifically R/C soaring. The interest in designing such a series was motivated by the results of a survey taken at the 1996 AMA Nationals/Unlimited Thermal Soaring Competition in which flight duration and landing precision were emphasized. The survey showed that of the 101 responses (from nearly all of the participants) 40 of the pilots used the SD7037 airfoil[14] (shown in Fig. 1 together with its velocity distribution). Two other airfoils (S3021 and RG15) each numbered 8 in use, followed by the fourth (SD7080) with 6, and then 24 different airfoils were used on the remainder. Despite the overwhelming popularity of the SD7037, it was obvious that this airfoil could not be the optimum for a wide range of sailplanes with different sizes, wing loadings, and weather conditions. For example, in some situations pilots would benefit by having a faster version of the SD7037 (lower lift), and in others a slower version (higher lift) might be preferable. Thus, the SD7037 became the baseline for this first series.

For the series, the objective was to produce a range of similar performing airfoils that differed with respect to their lift range. One approach would be to make simple camber changes to the SD7037 to arrive at the new airfoils, but this process was not used because it is more attractive to control the performance by using the inverse capabilities in PROFOIL. In particular, PROFOIL was used to set the lower corner of the polar by specifying that the laminar boundary layer on the lower surface be close to separating at the lift coefficient at the lower corner of the polar. The shape of the polar above this lift coefficient was then obtained by tailoring the aerodynamics of the upper surface, which is discussed later.

Figure 2 shows the particular laminar boundary-layer development prescribed for the lower corner of the polar. This boundary-layer shape parameter H_{12} distribution, which is close to laminar separation, was specified to be achieved at the design angles of attack of 1.75, 2.15, 2.55, and 2.95 deg relative to the zero-lift

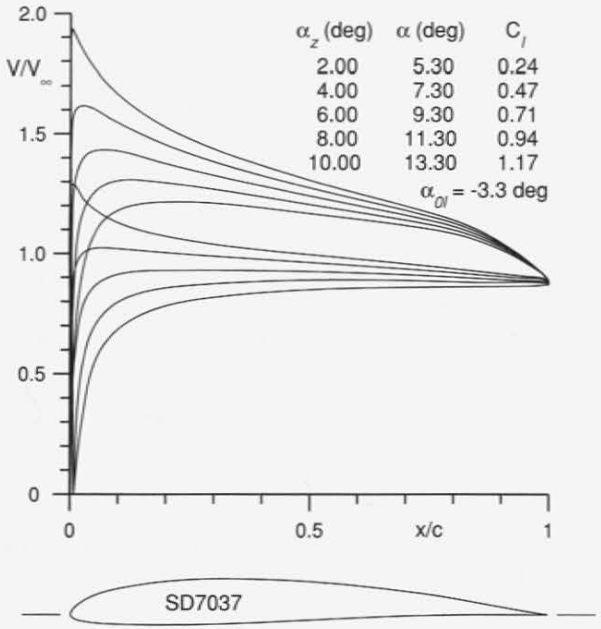

Fig. 1 SD7037 airfoil and inviscid velocity distributions.

line to produce each respective airfoil of the SA703x series shown in Fig. 3. (The SA7037 mimics the baseline SD7037.) In the figure, the velocity distributions are plotted at angle of attack increments equal to those that separate the aforementioned lower surface design angles of attack. The corresponding boundary-layer shape parameter developments as predicted by XFOIL for the lower surface design condition are shown in Fig. 4, and they are practically identical to the prescription shown in Fig. 2.

It is worth noting that the laminar boundary-layer H_{12} developments are plotted for a Reynolds number of 200,000; however, the laminar development to transition is independent of the Reynolds number, as discussed in Ref. 4. Also, although the

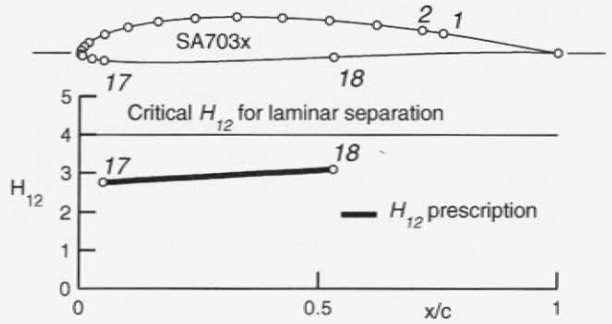

Fig. 2 Lower-surface laminar boundary-layer development prescribed for the SA703x airfoil series for the lower corner of the drag polar.

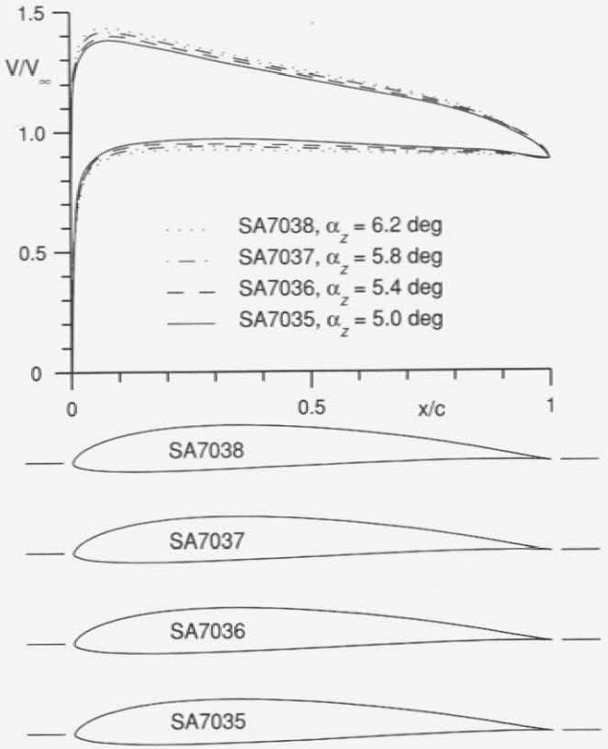

Fig. 3 SA703x airfoils and inviscid velocity distributions.

design specification was for there to be laminar flow on this segment at the design condition, in application the Reynolds number could quite well be off-design and cause transition before the end of this segment when operating at the design lift coefficient of the lower surface. Nevertheless, the prescription serves to define the lower-surface velocity distribution and corresponding geometry.

When each airfoil is operated below the respective design angle of attack for the lower surface, laminar separation and subsequent transition in the laminar-separation bubble quickly move forward and lead to higher drag at the end of the

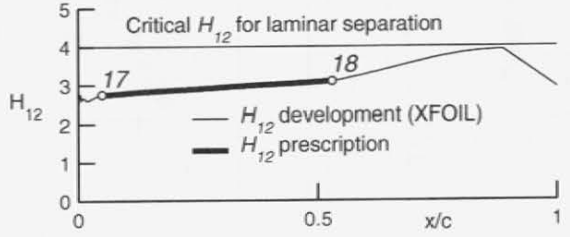

Fig. 4 Laminar boundary-layer development achieved for the SA703x airfoils and the agreement with the prescription.

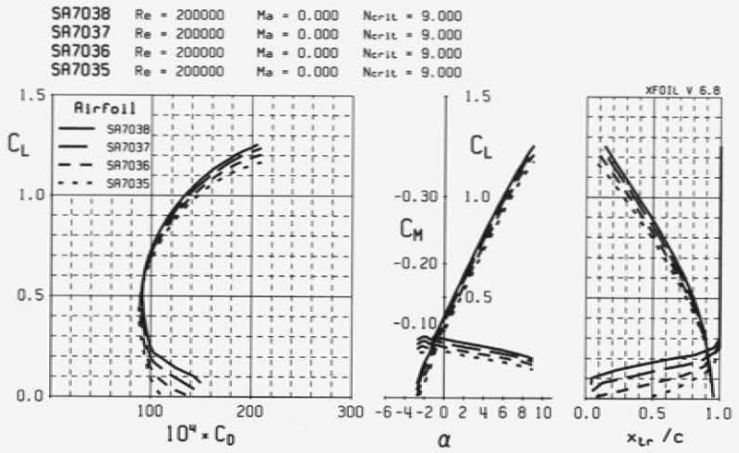

Fig. 5 XFOIL predictions for the SA703x airfoil series.

low-drag range. This result is found in the predictions of XFOIL shown in Fig. 5 and validated by the wind tunnel test results shown in Fig. 6. (In place of the SA7037, the baseline SD7037 was tested.) Additional data for these airfoils over the Reynolds number range from 100,000 to 300,000 can be found in Ref. 18, and tabulated data are available online at http://www.uiuc.edu/ph/www/m-selig (cited September 2001).

Of critical importance in the design of low Reynolds number airfoils is the upper-surface pressure distribution. The tendency of the flow to form a laminar-separation bubble can lead to a significant degradation in performance owing to

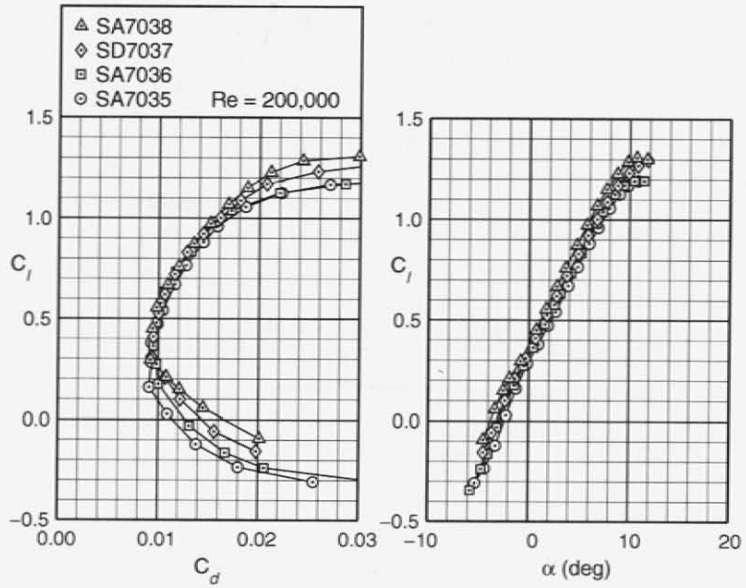

Fig. 6 Measured drag polars for the SA703x airfoil series.

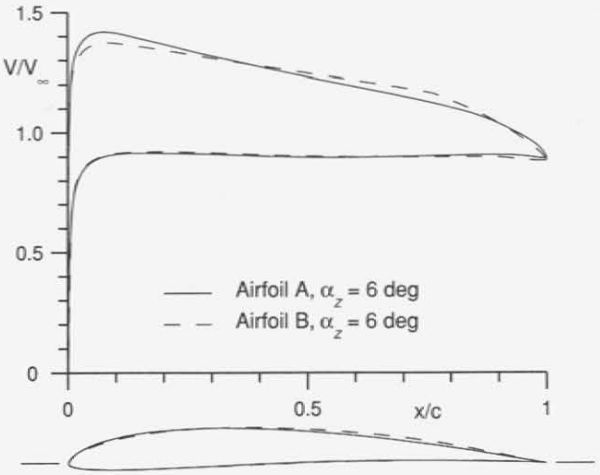

Fig. 7 Inviscid velocity distributions for airfoils A and B to study the different effects on drag.

the high bubble drag. To mitigate these adverse effects, a transition ramp in the pressure distribution is often employed to gradually bring the flow to transition in a thin bubble without a large pressure rise and high drag associated with an otherwise thick bubble. A general discussion of transition ramps can be found in Refs. 4 and 26, and additional details specific to low Reynolds number airfoils are discussed in Refs. 13, 14, 27, and 28.

The effect of the transition ramp is demonstrated using two example airfoils A and B. Figure 7 shows a comparison of the geometries and inviscid velocity distributions. These airfoils were designed using PROFOIL to each have a different transition ramp that is reflected in a different shape for the transition curve (C_l–x_{tr}/c curve) on the upper surface. The two airfoils were analyzed using XFOIL, and Fig. 8 shows the drag polars and upper-surface transition curves for a Reynolds number of 200,000. For the sake of discussion, the transition ramp is defined here as the region over which the bubble moves gradually as defined by the transition curve. (In this context, the transition ramp might be more aptly called a "bubble ramp."[14])

From the figure, it can be seen that airfoil A has lower drag than airfoil B at lift coefficients from around 0.3 to around 0.7, above which value airfoil B has lower drag. Also noticeable is the correlation between the drag polar and the shape of the upper-surface transition curve. For the C_l range from 0.3 to 0.7, where airfoil A has lower drag, the transition curve for airfoil A is shallower than that for airfoil B; that is, there is a larger change in the value of x_{tr}/c for airfoil A than for B. For values of C_l from 0.7 to 1.2 where airfoil B has lower drag, the transition curve for airfoil B is shallower than for A. This figure shows that the steepness of the transition curve is a direct indication of the bubble drag. By adjusting the shape of this curve, it is therefore possible to tailor the drag polar of an airfoil at low Reynolds numbers.

Figure 8 also includes an overlay of the variation of bubble size ($x_r - x_s$) with C_l. The size of the bubble for each C_l was obtained by determining the chordwise extent over which the skin friction C_f, as predicted by XFOIL, was less than

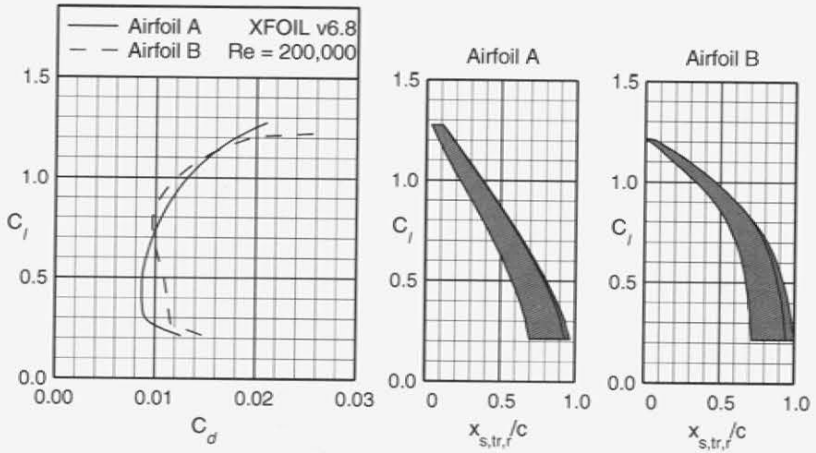

Fig. 8 XFOIL predictions for airfoils A and B to illustrate the effects of changes in the transition ramp on drag.

or equal to zero. Studying the bubble-size variation for the two airfoils further illustrates the connection between the shape of the transition curve and the bubble drag. The bubble is larger when the transition curve is steeper.

Figure 9 shows the inviscid velocity distributions for airfoil A at C_l values of 0.5 and 1.0 with the upper-surface bubble location marked in bold. A similar plot for airfoil B is shown in Fig. 10. Comparing the velocity drops across the bubble for the four cases, it can be seen that although airfoil A has a smaller velocity

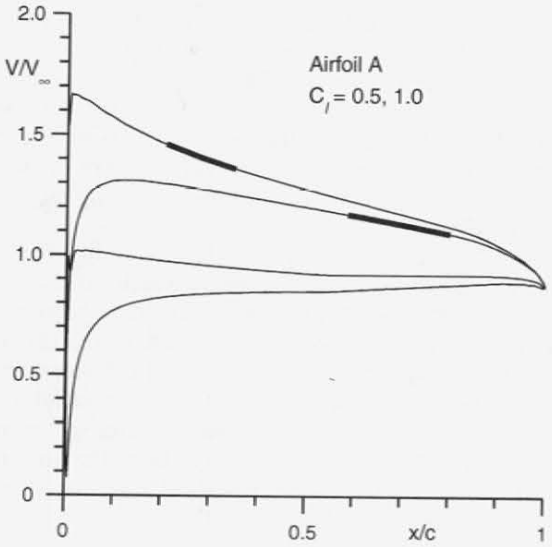

Fig. 9 Inviscid velocity distributions for airfoil A with the locations of the bubble marked.

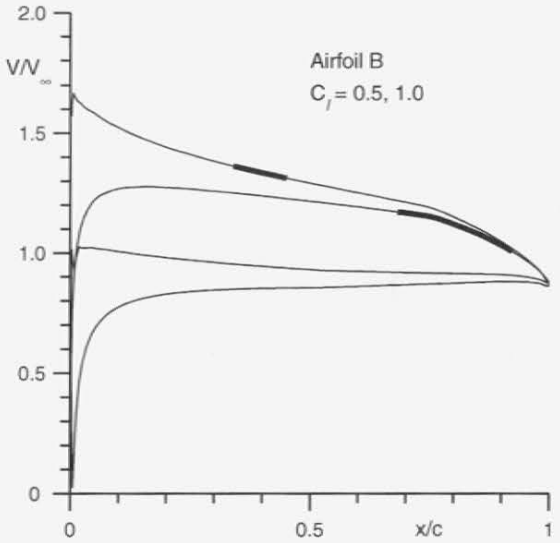

Fig. 10 Inviscid velocity distributions for airfoil B with the locations of the bubble marked.

drop than airfoil B at $C_l = 0.5$, the situation is reversed for $C_l = 1.0$. Because the pressure drag caused by the bubble increases with increasing velocity drop across the bubble, airfoil A has smaller bubble drag at the low C_l and larger bubble drag at the higher C_l. Thus, a steeper transition curve results in a larger bubble and also larger velocity drop across the bubble causing an increase in bubble drag.

Understanding the connection between the transition ramp in the velocity distribution, the C_l–x_{tr}/c transition curve, and the performance is the first step to obtaining optimum low Reynolds number airfoil design. The next step in design involves the implementation of these ideas. In studying the velocity distributions shown in Figs. 3 and 7 and the resulting behavior of the transition curves shown in Figs. 5 and 8, respectively, we see that the connection between the two is not straightforward owing to the subtle (yet important) differences. Moreover, it is worth adding that the differences in the airfoil shape are even less useful in guiding the design toward an optimum with respect to the transition ramp and its impact on drag.

In coping with this problem, a useful approach derives from an inherent feature of the Eppler theory for inverse airfoil design. Briefly, in the Eppler method, the designer can specify for a segment of the airfoil a design angle attack α^* (relative to the zero-lift line) over which the velocity is constant. For instance, the forward upper surface can be defined as one segment and given a design angle of attack of 10 deg ($C_l = 2\pi\alpha_z \sim 1$). When the resulting airfoil is then operated at 10 deg with respect to the zero-lift angle of attack α_{zl}, the velocity over that segment is then constant. For a higher angle of attack, the resulting pressure gradient is adverse and vice versa. Further discussion can be found in Refs. 4 and 29.

Because 1) the boundary layer responds to the pressure gradient, 2) the design angle of attack α^* for a segment has a direct effect on the pressure gradient, and 3) many such segments can be used to define an airfoil, these three aspects can be

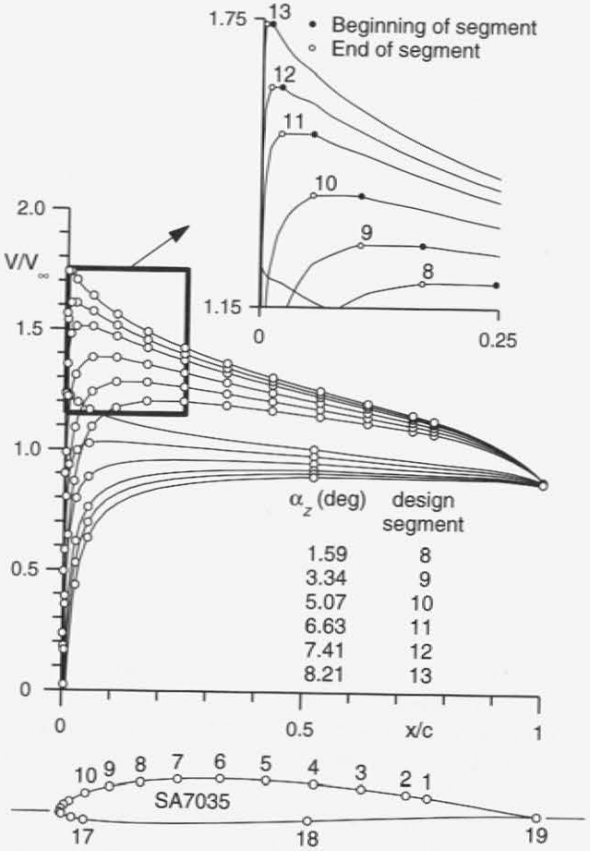

Fig. 11 SA7035 inviscid velocity distributions showing the zero pressure-gradient segments and corresponding design angles of attack.

connected to yield an elegant solution to having precise control over the C_l–x_{tr}/c transition curve. Figure 11 shows the velocity distributions for the SA7035 airfoil at several design angles of attack. As seen, for segments 8, 9, 10, 11, 12, and 13 the design angles of attack α^* are 1.59, 3.34, 5.07, 6.63, 7.41, and 8.21 deg, respectively. When the airfoil operates at these values of α_z, the velocity gradient over the respective segments is zero, as shown in the exploded portion of the figure. When these design angles of attack α^* are plotted vs the segment-endpoint arc limits ϕ used in the conformal mapping to generate the airfoil, the resulting curves shown in Fig. 12 mimic the corresponding transition curves (duplicated from Fig. 5) over the respective surface of the airfoil, thereby providing a means of controlling the transition ramp and resulting drag as was done also with the example of Figs. 7 and 8. For the SA703x series, the α^*–ϕ curve shown in Fig. 12 maps from leading edge back to segment-endpoint 1 or approximately 75% of the chord (see Fig. 11). It is over this region that the ramp is controlled by the α^*–ϕ curve, with the remainder being controlled by the final trailing-edge pressure recovery seen in Fig. 11. The essence of this technique has been employed in the design of most of the S*xxxx four-digit airfoils reported in the literature

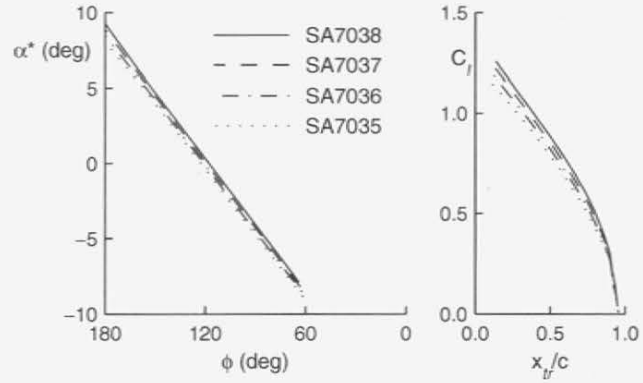

Fig. 12 Linkage between the α^*–ϕ and C_l–x_{tr} curves for the SA703x airfoil series.

and archived online at http://www.uiuc.edu/ph/www/m-selig (cited September 2001) and in Refs. 14, 16, 17, 18, and 30.

B. SG604x Series

The SG604x series of airfoils[31] as shown in Fig. 13 was designed for small variable-speed horizontal-axis wind turbines having a rated power of 1–5 kW. The operational Reynolds number for such machines is typically below 10^6. The focus here will be on the performance at a Reynolds number of 300,000, which represents rotors on the lower end of the range. In ideal conditions, variable-speed wind turbines operate at a constant tip-speed-ratio ($\Omega R/V_\infty$), which leads to the airfoil operating at a single angle of attack over a wide range of wind speeds. As a result, for optimum aerodynamic performance during variable-speed operation, the low-drag lift range (drag bucket) can be reduced in favor of having greater lift-to-drag ratios. However, to account for possible variations in the tip-speed-ratio caused by atmospheric turbulence and operational considerations, the best lift-to-drag ratio conditions should occur over a range of lift coefficients centered about the design lift coefficient. In rotor design, another factor deals with the tradeoff between the blade solidity and the design lift coefficient. With all else being equal, a high-solidity rotor requires an airfoil with lower lift than that required for a low-solidity rotor. Therefore, given the range of rotor designs, a family of airfoils covering a range of lift coefficients is desirable. These general considerations and others were taken into account in setting the design requirements, as detailed more thoroughly in Ref. 31. The current discussion is mainly concerned with the details of the design approach.

Again PROFOIL was used to prescribe the desired aerodynamic characteristics. In a manner similar to that used in the previously discussed SA703x series, the boundary-layer shape parameter was prescribed on the lower surface to control the lower corner of the low-drag range of the polar. In this respect, there were some minor differences in the prescriptions, but generally a similar behavior was obtained. The transition ramp on the upper surface differs from that of the SA703x series in much the same way that airfoil B differs from airfoil A in Fig. 7. Since the objective was to achieve a high lift-to-drag ratio with less emphasis being given to operation over a wide range, the ramp on the upper surface was made more shallow

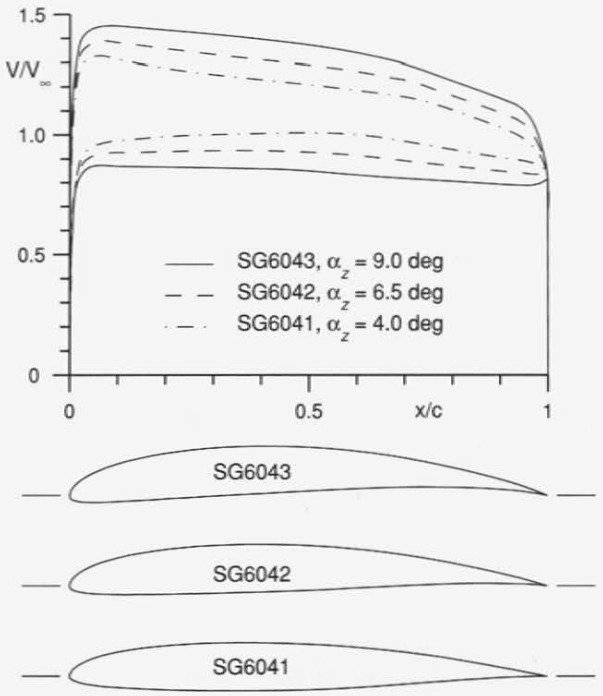

Fig. 13 SG604x airfoils and inviscid velocity distributions.

at the specific design lift coefficients of 0.6, 0.9, and 1.2 for the SG6041, SG6042, and SG6043, respectively. As before, the transition curve was controlled through the shape of the $\alpha^*-\phi$ curve shown in Fig. 14. Additional constraints included the pitching moment, which increased with the design lift coefficient, and also the airfoil thickness of 10%. It should be added that for ease of construction a finite trailing-edge angle was used, producing a zero trailing-edge velocity as seen in Fig. 13.

Performance predictions at a Reynolds number of 300,000 are shown in Fig. 15 and compare relatively well with the experimental results of Fig. 16. Most importantly, the trends in the predictions agree well with experiment, and also the behavior of the $\alpha^*-\phi$ curve is reflected in the transition curve.

Figure 17 shows the resulting experimentally determined lift-to-drag ratios at a Reynolds number of 300,000 compared with those for many previously existing airfoils. The SG6040 shown in the figure is the thicker companion root airfoil for the series of tip airfoils discussed here. Clearly, the objective of achieving high lift-to-drag ratios has been achieved. Given the high level of performance, these airfoils will likely find their way into applications beyond wind energy.

C. S607x Series

In contrast to the first two series, the S607x series is composed of three series of three airfoils each. The effort finally led to an airfoil for its intended application

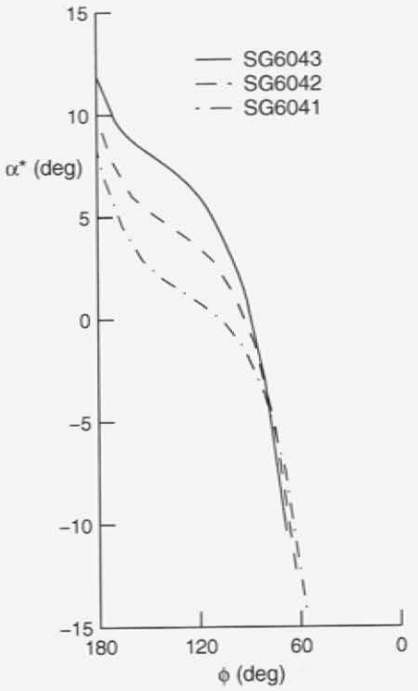

Fig. 14 SG604x airfoil series $\alpha^*-\phi$ curves for control over the C_l-x_{tr} curves.

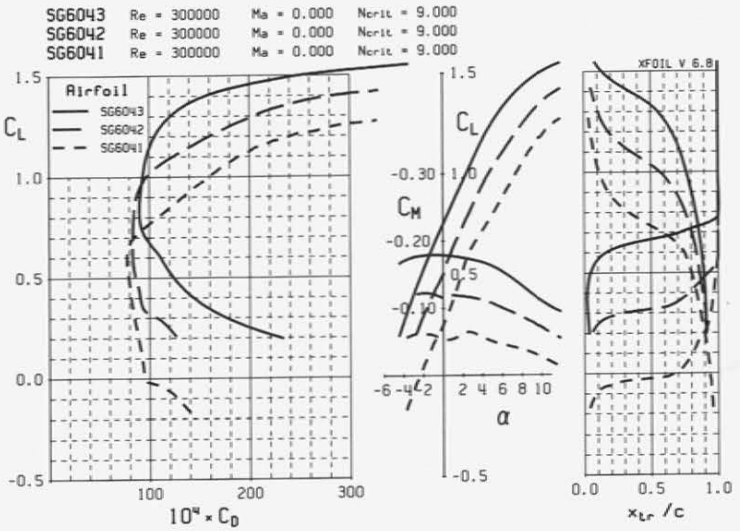

Fig. 15 XFOIL predictions for the SG604x airfoil series.

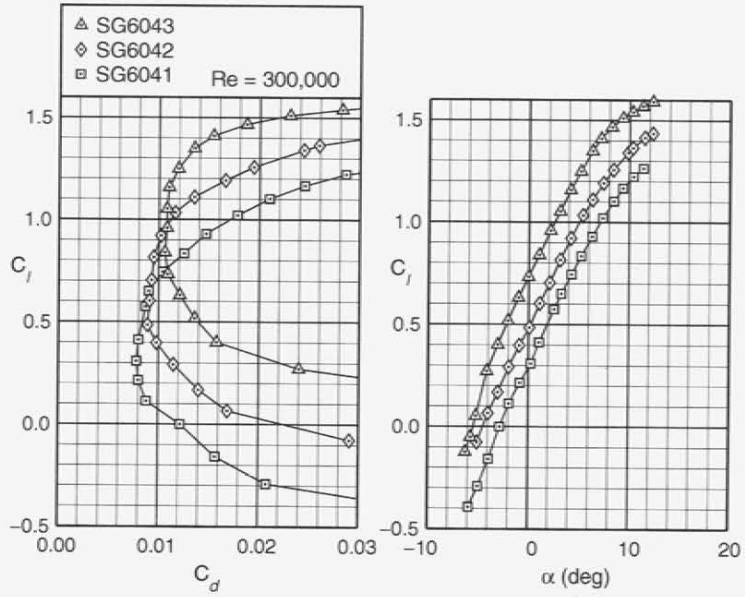

Fig. 16 Measured drag polars for the SG604x airfoil series.

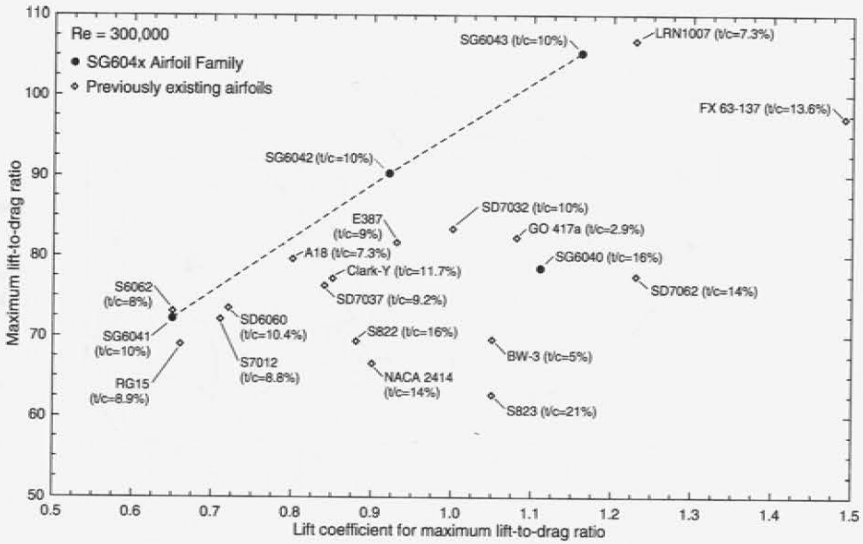

Fig. 17 Maximum lift-to-drag ratio vs the corresponding lift coefficient for the SG604x airfoil series compared with several previously existing airfoils.

that required a low pitching moment and optimum performance at a Reynolds number of 150,000 and lift coefficient near 1. Only data for a Reynolds number of 200,000 are presented here, however. The series evolved from a 9%-thick family to a 12%-thick one, and then permutations in the pitching moment were made while other improvements were incorporated. The series will be discussed in this order.

As in the prior examples, the lower surface of each airfoil was designed by prescribing the boundary-layer shape parameter development at its respective design angle of attack. For the first series S6071/2/3, the study centered on the upper-surface transition ramp. Figure 18 shows that small changes in the $\alpha^* - \phi$ curve affect the transition ramp, making it more shallow in going from airfoil S6071 to S6073. These differences result in small changes to the resulting velocity distributions shown in Fig. 19. As seen, the shallower $\alpha^* - \phi$ curve for airfoil S6073 results in a shallower pressure gradient over the forward upper surface. The differences in the airfoil shapes are so minute that a magnification of the y axis is needed to highlight the differences, as shown in Fig. 20. These small changes to the ramp, however, do have a significant effect on the bubble, as may be deduced by the drag predictions shown in Fig. 21. Wind tunnel tests depicted in Figs. 22 and 23 confirm the predicted trends.

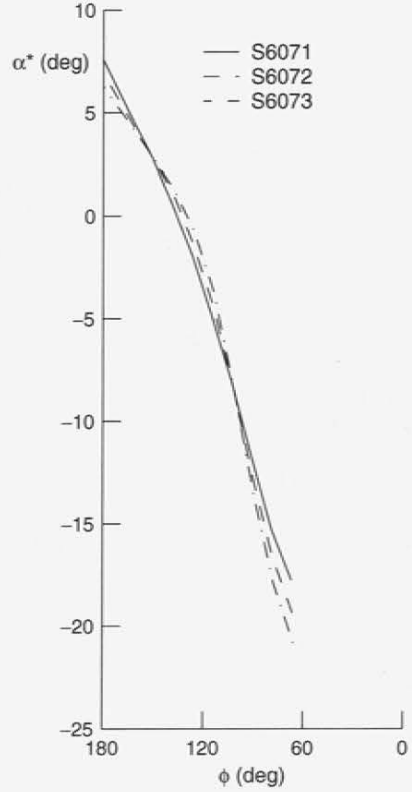

Fig. 18 S6071/2/3 airfoil series $\alpha^* - \phi$ curves for control over the $C_l - x_{tr}$ curves.

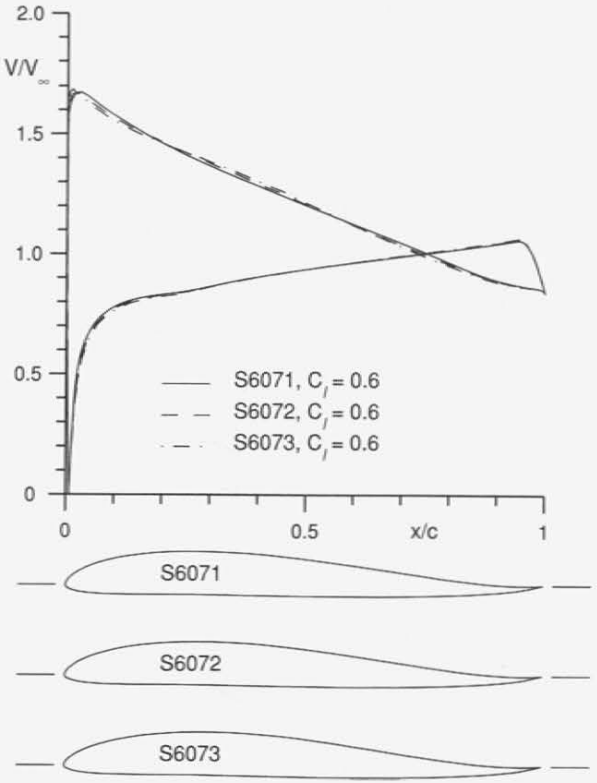

Fig. 19 S6071/2/3 airfoils and inviscid velocity distributions.

The next perturbation included largely a change in the airfoil thickness from 9% to 12%. Figure 24 shows the two bounding airfoils S6074/6 and their corresponding velocity distributions. Again the differences appear minor; however, as seen in Fig. 25 the trends are similar to the prior series, albeit with there being higher drag owing to the higher airfoil thickness. XFOIL predictions indicated similar increases in drag.

The wind tunnel tests of the S6074/5/6 airfoils revealed an undesirable feature of the series—stall hysteresis as shown Fig. 26, which was also found on airfoil S6071. Such hysteresis cannot be predicted by any method currently available. This type of hysteresis, however, has been found on other airfoils. As described in

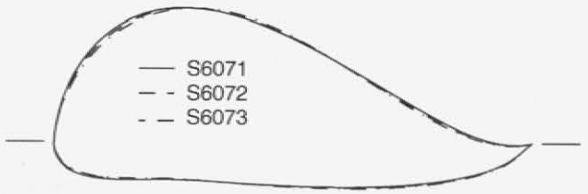

Fig. 20 S6071/2/3 airfoils with the thickness magnified to show the small differences.

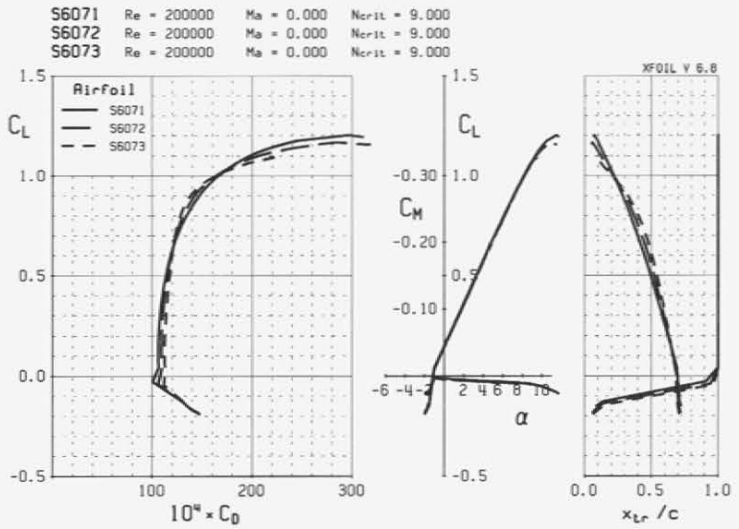

Fig. 21 XFOIL predictions for the S6071/2/3 airfoils.

Ref. 13, when the inviscid velocity distribution on the forward upper surface tends toward a concave shape, stall hysteresis of the type found here can be reduced. Unfortunately, no computational tool exists to quantify this effect, and the degree to which the pressure distribution (or velocity distribution) should tend in the concave direction has not been quantified. Nevertheless, the chief aim of the final series was to eliminate this hysteresis.

Figure 27 shows the two bounding airfoils S6077/9 designed to avoid stall hysteresis while satisfying the other constraints. A secondary purpose of this final

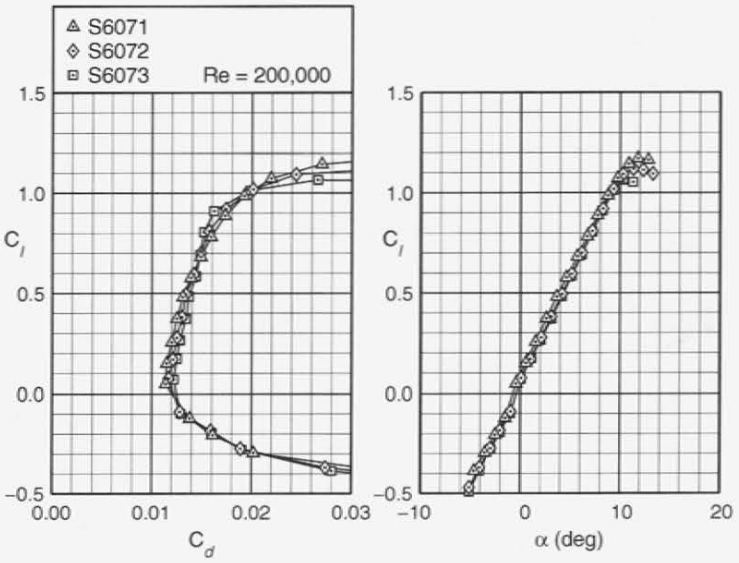

Fig. 22 Measured drag polars for the S6071/2/3 airfoils.

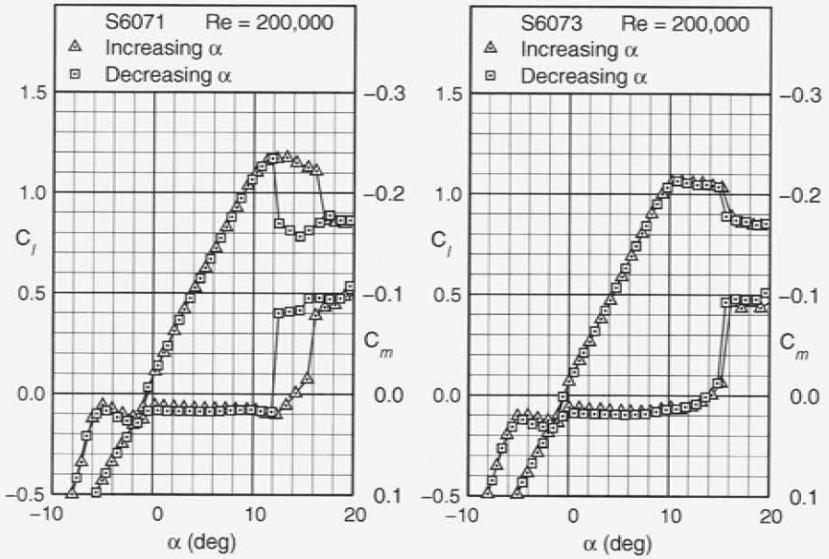

Fig. 23 Measured lift curves for the S6071/3 airfoils.

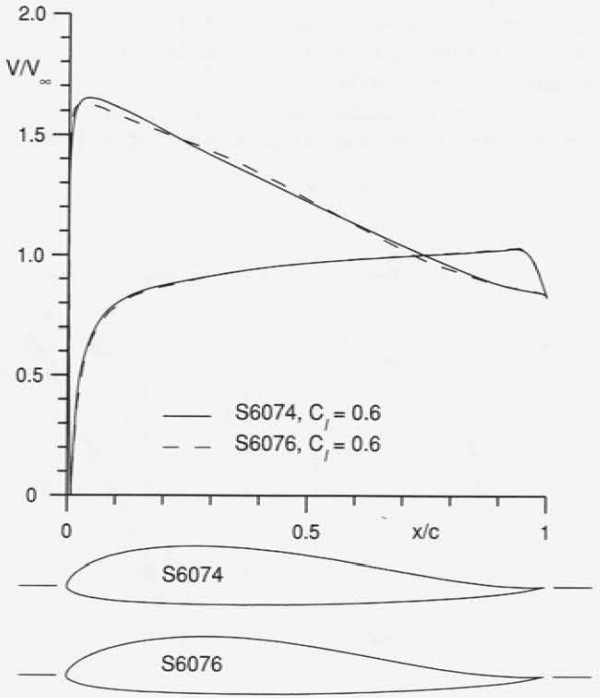

Fig. 24 S6074/6 airfoils and inviscid velocity distributions.

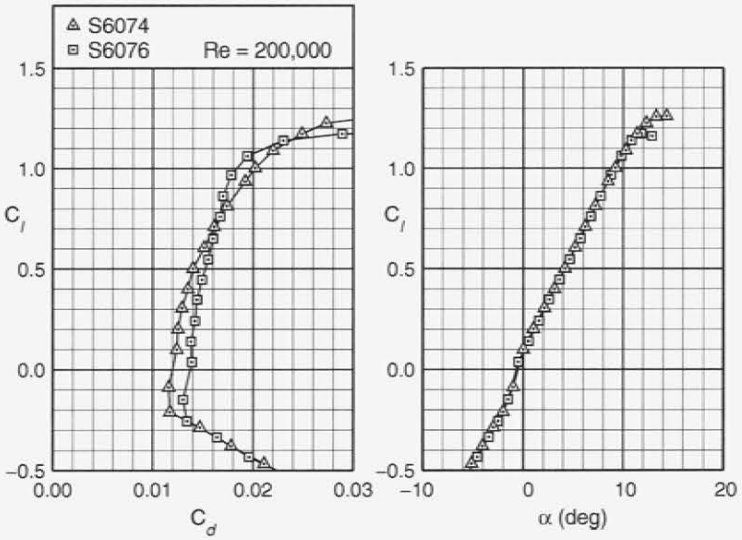

Fig. 25 Measured drag polars for the S6074/6 airfoils.

series was to examine the effects of a change in the pitching moment, which was specified using the inverse capabilities of PROFOIL. In comparing the velocity distributions shown in Fig. 24 with those in Fig. 27 it is seen that this current series has a more concave velocity distribution on the forward upper surface, and this difference is reflected in the shapes of the S6074/6 vs S6077/9 shown in Fig. 28. As seen in Fig. 29, this change in the velocity distribution is enough to eliminate the stall hysteresis. Finally, the performance is shown in Fig. 30. One feature of

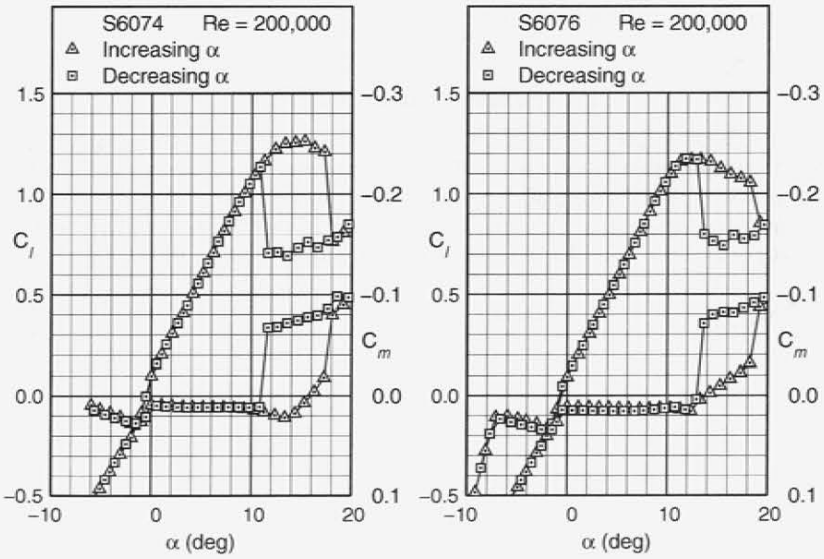

Fig. 26 Measured lift curves for the S6074/6 airfoils.

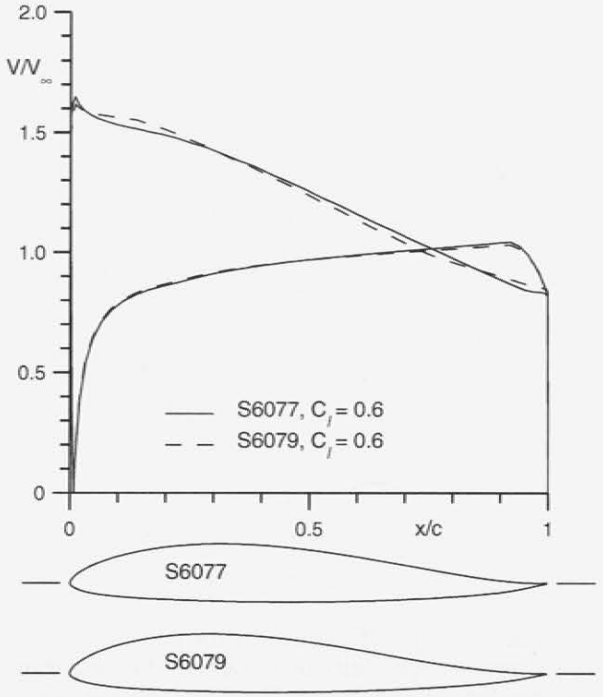

Fig. 27 S6077/9 airfoils and inviscid velocity distributions.

using a more concave distribution is that the $\alpha^* - \phi$ curve (not shown) becomes more shallow. As a result, the laminar-separation bubble drag is reduced at the upper corner of the low-drag range, yielding lower drag than the S6074/6 but also lower maximum lift as a tradeoff.

IV. Summary and Conclusions

In this chapter, three series of airfoils were designed to illustrate the power of modern computational tools for low Reynolds number airfoil design and analysis. Emphasis was placed on the design of the airfoils based on boundary-layer considerations. More specifically, the parameterization of the design problem centered around prescribing desirable boundary-layer features directly through an inverse

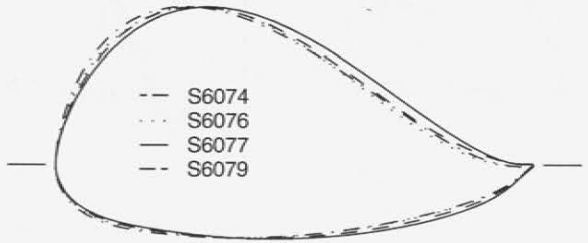

Fig. 28 S6074/6/7/9 airfoils with the thickness magnified to show the small differences.

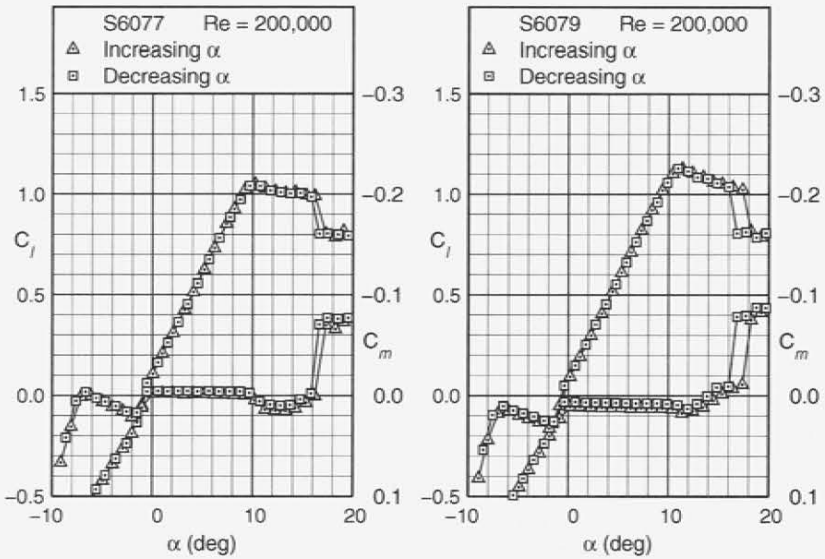

Fig. 29 Measured lift curves for the S6077/9 airfoils.

method. Formulating the design problem in this way offers the designer considerably more power than one would otherwise have using more traditional methods of inverse design (based on a single-point velocity distribution) and design by geometric perturbation. The design approach and philosophy can be used successfully to assess design tradeoffs with a high degree of control. Finally, wind-tunnel testing of low Reynolds number airfoils is, however, still needed to provide engineers with a necessary level of confidence required to make important engineering decisions.

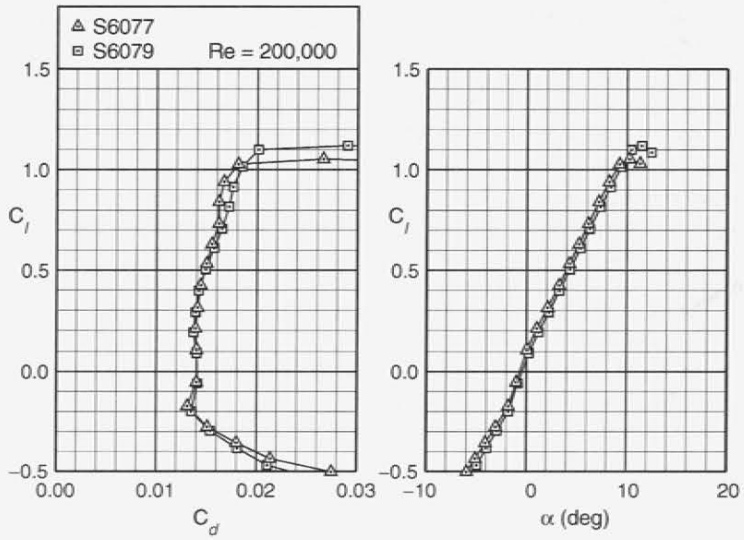

Fig. 30 Measured drag polars for the S6077/9 airfoils.

Acknowledgments

Funding for this work was provide through a variety of sources for which we are grateful, namely, private donations (see Refs. 16, 17, and 18 for individual listings), the National Renewable Energy Laboratory, and AeroVironment. Also, we thank all the model makers, Mark Allen, Allen Developments (SA7035, SG604x); Tim Foster and Frank Carson (SA7038); Jerry Robertson (SD7037); D'Anne Thompson (SA7036); and Yvan Tinel, Tinel Technologies (S607x series), for their meticulous and skillful efforts in model construction. The authors also wish to thank Mark Drela for providing the XFOIL code used in this work.

References

[1]Selig, M. S., and Maughmer, M. D., "A Multi-Point Inverse Airfoil Design Method Based on Conformal Mapping," *AIAA Journal*, Vol. 30, No. 5, May 1992, pp. 1162–1170.

[2]Selig, M. S., and Maughmer, M. D., "Generalized Multipoint Inverse Airfoil Design," *AIAA Journal*, Vol. 30, No. 11, Nov. 1992, pp. 2618–2625.

[3]Eppler, R. and Somers, D. M., "A Computer Program for the Design and Analysis of Low-Speed Airfoils," NASA TM 80210, Aug. 1980.

[4]Eppler, R., *Airfoil Design and Data*, Springer-Verlag, New York, 1990.

[5]Drela, M., "XFOIL: An Analysis and Design System for Low Reynolds Number Airfoils," *Low Reynolds Number Aerodynamics*, edited by T. J. Mueller, Vol. 54 of *Lecture Notes in Engineering*, Springer-Verlag, New York, June 1989, pp. 1–12.

[6]Eppler, R., "Direkte Berechnungvon Tragflugelprofilen aus der Druckverteilung," *Ingenieur-Archive*, Vol. 25, No. 1, 1957, pp. 32–57 (translated as "Direct Calculation of Airfoil from Pressure Distribution," NASA TT F-15, 417, 1974).

[7]Eppler, R., "Ergebnisse gemeinsamer Anwendung vo Grenzschicht- und Potentialtheorie," *Zeitschrift für Flugwissenschaften*, Vol. 8, No. 9, 1960, pp. 247–260 (translated as "Results of the Combined Application of Boundary Layer and Profile Theory," NASA TT F-15, 416, March 1974).

[8]Selig, M. S., "Multi-Point Inverse Design of Isolated Airfoils and Airfoils in Cascade in Incompressible Flow," Ph.D. Thesis, Pennsylvania State Univ., State College, PA, May 1992.

[9]Thies, W., *Eppler-Profile*, MTB 1, Verlag für Technik und Handwerk, Baden-Baden, Germany, 1981 (republished, Hepperle, M., MTB 1/2, 1986).

[10]Thies, W., *Eppler-Profile*, MTB 2, Verlag für Technik und Handwerk, Baden-Baden, Germany, 1982 (republished, Hepperle, M., MTB 1/2, 1986).

[11]Althaus, D., *Profilpolaren für den Modellflug—Windkanalmessung an Profilen im Kritischen Reynoldszahlbereich*, Neckar-Verlag, Villingen-Schwenningen, Germany, 1980.

[12]Althaus, D., *Profilpolaren für den Modellflug—Windkanalmessung an Profilen im Kritischen Reynoldszahlbereich*, Band 2, Neckar-Verlag, Villingen-Schwenningen, Germany, 1985.

[13]Selig, M. S., "The Design of Airfoils at Low Reynolds Numbers," AIAA Paper 85-0074, Jan. 1985.

[14]Selig, M. S., Donovan, J. F., and Fraser, D. B., *Airfoils at Low Speeds, Soartech 8*, SoarTech Publications, Virginia Beach, VA, 1989.

[15]Hepperle, M., *Neue Profile für Nurflügelmodelle*, FMT-Kolleg 8, Verlag für Technik und Handwerk GmbH, Baden-Baden, Germany, 1988 (republished, Hepperle, M., MTB 1/2, 1986).

[16]Selig, M. S., Guglielmo, J. J., Broeren, A. P., and Giguère, P., *Summary of Low-Speed Airfoil Data*, Vol. 1, SoarTech Publications, Virginia Beach, VA, 1995.

[17]Selig, M. S., Lyon, C. A., Giguère, P., Ninham, C. N., and Guglielmo, J. J., *Summary of Low-Speed Airfoil Data*, Vol. 2, SoarTech Publications, Virginia Beach, VA, 1996.

[18]Lyon, C. A., Broeren, A. P., Giguère, P., Gopalarathnam, A., and Selig, M. S., *Summary of Low-Speed Airfoil Data*, Vol. 3, SoarTech Publications, Virginia Beach, VA, 1998.

[19]Guglielmo, J. J., and Selig, M. S., "Spanwise Variations in Profile Drag for Airfoils at Low Reynolds Numbers," *Journal of Aircraft*, Vol. 33, No. 4, July–Aug. 1996, pp. 699–707.

[20]Guglielmo, J. J., "Spanwise Variations in Profile Drag for Airfoils at Low Reynolds Numbers," M.S. Thesis, Dept. of Aeronautical and Astronautical Engineering, Univ. of Illinois at Urbana–Champaign, Urbana, IL, 1995.

[21]Rae, W. H., Jr. and Pope, A., *Low-Speed Wind Tunnel Testing*, Wiley, New York, 1984.

[22]Giguère, P., and Selig, M. S., "Freestream Velocity Measurements for Two-Dimensional Testing with Splitter Plates," *AIAA Journal*, Vol. 35, No. 7, July 1997, pp. 1195–1200.

[23]McGhee, R. J., Walker, B. S., and Millard, B. F., "Experimental Results for the Eppler 387 Airfoil at Low Reynolds Numbers in the Langley Low-Turbulence Pressure Tunnel," NASA TM 4062, Oct. 1988.

[24]Coleman, H. W., and Steele, W. G., Jr., *Experimentation and Uncertainty Analysis for Engineers*, Wiley, New York, 1989.

[25]Lyon, C. A., Selig, M. S., and Broeren, A. P., "Boundary Layer Trips on Airfoils at Low Reynolds Numbers," AIAA Paper 97-0511, Jan. 1997.

[26]Wortmann, F. X., "Progress in the Design of Low Drag Airfoils," *Boundary Layer and Flow Control*, edited by G. V. Lachmann, Pergamon, London, 1961, pp. 748–770.

[27]Donovan, J. F., and Selig, M. S., "Low Reynolds Number Airfoil Design and Wind Tunnel Testing at Princeton University," *Low Reynolds Number Aerodynamics*, edited by T. J. Mueller, Vol. 54 of *Lecture Notes in Engineering*, Springer-Verlag, New York, June 1989, pp. 39–57.

[28]Drela, M., "Low Reynolds-Number Airfoil Design for the M.I.T. Daedalus Prototype: A Case Study," *Journal of Aircraft*, Vol. 25, No. 8, Aug. 1988, pp. 724–732.

[29]Gopalarathnam, A., and Selig, M. S., "Low-Speed Natural-Laminar-Flow Airfoils: Case Study in Inverse Airfoil Design," *Journal of Aircraft*, Vol. 38, No. 1, Jan.–Feb. 2001, pp. 57–63.

[30]Selig, M. S., *The Design of Airfoils at Low Reynolds Numbers, Soartech 3*, SoarTech Publications, Virginia Beach, VA, 1984.

[31]Giguère, P., and Selig, M. S., "New Airfoils for Small Horizontal Axis Wind Turbines," *ASME Journal of Solar Energy Engineering*, Vol. 120, May 1998, pp. 108–114.